

Hybrid particle swarm global optimization algorithm for phase diversity phase retrieval

P. G. ZHANG,¹ C. L. YANG,^{1,3} Z. H. XU,^{1,2} Z. L. CAO,¹ Q. Q. MU,^{1,4}
AND L. XUAN¹

¹State Key Laboratory of Applied Optics, Changchun Institute of Optics, Fine Mechanics and Physics (CIOMP), Chinese Academy of Sciences, 130033, Changchun, Jilin, China

²Graduate School of the Chinese Academy of Sciences, Beijing 100039, China

³ycldahai@ciomp.ac.cn

⁴muquanquan@ciomp.ac.cn

Abstract: The core problem of phase diversity phase retrieval (PDPR) is to find suitable optimization algorithms for wave-front sensing of different scales, especially for large-scale wave-front sensing. When dealing with large-scale wave-front sensing, existing gradient-based local optimization algorithms used in PDPR are easily trapped in local minimums near initial positions, and available global optimization algorithms possess low convergence efficiency. We construct a practicable optimization algorithm used in PDPR for large-scale wave-front sensing. This algorithm, named EPSO-BFGS, is a two-step hybrid global optimization algorithm based on the combination of evolutionary particle swarm optimization (EPSO) and the Broyden-Fletcher-Goldfarb-Shanno (BFGS) algorithm. Firstly, EPSO provides global search and obtains a rough global minimum position in limited search steps. Then, BFGS initialized by the rough global minimum position approaches the global minimum with high accuracy and fast convergence speed. Numerical examples testify to the feasibility and reliability of EPSO-BFGS for wave-front sensing of different scales. Two numerical cases also validate the ability of EPSO-BFGS for large-scale wave-front sensing. The effectiveness of EPSO-BFGS is further affirmed by performing a verification experiment.

© 2016 Optical Society of America

OCIS codes: (010.7350) Wave-front sensing; (100.5070) Phase retrieval; (100.3010) Image reconstruction techniques; (000.3860) Mathematical methods in physics.

References and links

1. D. J. Lee, B. M. Welsh, M. C. Roggemann, and B. L. Ellerbroek, "Diagnosing unknown aberrations in an adaptive optics system by use of phase diversity," *Opt. Lett.* **22**(13), 952–954 (1997).
2. R. G. Paxman, B. J. Thelen, and J. H. Seldin, "Phase-diversity correction of turbulence-induced space-variant blur," *Opt. Lett.* **19**(16), 1231–1233 (1994).
3. V. Korkiakoski, C. Keller, N. Doelman, R. Fraanje, and M. Verhaegen, "Joint-optimization of phase-diversity and adaptive optics," in *Imaging and Applied Optics*, (Optical Society of America, 2011), p.JTuC5.
4. J. J. Dolne, P. Menicucci, D. Miccolis, K. Widen, H. Seiden, F. Vachss, and H. Schall, "Real time phase diversity advanced image processing and wavefront sensing," in *Optical Engineering+ Applications* (International Society for Optics and Photonics, 2007).
5. R. A. Gonsalves, "Phase retrieval and diversity in adaptive optics," *Opt. Eng.* **21**(5), 829–832 (1982).
6. D. J. Lee, M. C. Roggemann, B. M. Welsh, and E. R. Crosby, "Evaluation of least-squares phase-diversity technique for space telescope wave-front sensing," *Appl. Opt.* **36**(35), 9186–9197 (1997).
7. N. Baba, H. Tomita, and N. Miura, "Iterative reconstruction method in phase-diversity imaging," *Appl. Opt.* **33**(20), 4428–4433 (1994).
8. A. Wirth, R. Gonsalves, and A. Jankevics, "Adaptive optics enabled wavefront diversity sensing," in *Imaging and Applied Optics*, (Optical Society of America, 2011), p.JTuC4.
9. V. Korkiakoski, C. U. Keller, N. Doelman, R. Fraanje, and M. Verhaegen, "Joint optimization of phase diversity and adaptive optics: demonstration of potential," *Appl. Opt.* **51**(1), 102–113 (2012).
10. I. Klapp and J. Rosen, "Phase diversity implementation in fresnel incoherent holography," in *Imaging and Applied Optics* (Optical Society of America, 2013), p.CTh3C.3.
11. N. Védrenne, L. M. Mugnier, V. Michau, M.-T. Velluet, and R. Bieri, "Laser beam complex amplitude measurement by phase diversity," *Opt. Express* **22**(4), 4575–4589 (2014).
12. N. Védrenne, F. Cassaing, L. M. Mugnier, V. Michau, G. Iaquaniello, L. Blanco, and G. Chériaux, "Design and performance of an integrated phase and amplitude diversity sensor," in *Conference on Lasers and Electro-Optics*

- (Optical Society of America, 2015), paper STu2N.2
13. P. Kner, "Phase diversity for three-dimensional imaging," *J. Opt. Soc. Am. A* **30**(10), 1980–1987 (2013).
 14. R. G. Paxman and J. R. Fienup, "Optical misalignment sensing and image reconstruction using phase diversity," *J. Opt. Soc. Am. A* **5**(6), 914–923 (1988).
 15. M. F. Fodsllette, "A scaled conjugate gradient algorithm for fast supervised learning," *Neural. Netw.* **6**(4), 525–533 (1993).
 16. X. Rondeau, E. Thiébaud, M. Tallon, and R. Foy, "Phase retrieval from speckle images," *J. Opt. Soc. Am. A* **24**(10), 3354–3365 (1988).
 17. P. M. Johnson, M. E. Goda, and V. L. Gamiz, "Multiframe phase-diversity algorithm for active imaging," *J. Opt. Soc. Am. A* **24**(7), 1894–1900 (2007).
 18. J. Zhong, L. Tian, P. Varma, and L. Waller, "Nonlinear optimization algorithm for partially coherent phase retrieval and source recovery," in *Proceedings of IEEE Transactions on Computational Imaging* (IEEE, 2016), pp. 99.
 19. L. Yeh, L. Tian, Z. Liu, M. Chen, J. Zhong and L. Waller, "Experimental robustness of Fourier Ptychographic phase retrieval algorithms," in *Imaging and Applied Optics 2015* (Optical Society of America, 2015), paper CW4E.2
 20. Y. Huizhen and L. Yaoqiu, "Genetic algorithm for phase retrieval of generalized phase diversity," *Energy Procedia* **13**, 4806–4811 (2011).
 21. K. James, "Particle swarm optimization," in *Encyclopedia of Machine Learning* (Springer, 2010)
 22. F. Van Den Bergh, "An analysis of particle swarm optimizers," Ph.D. thesis, University of Pretoria, (2006).
 23. R. C. Eberhart and K. James, "A new optimizer using particle swarm theory," in *Proceedings of the Sixth International Symposium on Micro Machine and Human Science* (New York, 1995), pp. 39–43.
 24. J. W. Goodman and S. C. Gustafson, "Introduction to fourier optics," *Opt. Eng.* **35**(5), 1513–1513 (1996).
 25. A. Blanc, L. M. Mugnier, and J. Idier, "Marginal estimation of aberrations and image restoration by use of phase diversity," *J. Opt. Soc. Am. A* **20**(6), 1035–1045 (2003).
 26. R. J. Noll, "Zernike polynomials and atmospheric turbulence," *J. Opt. Soc. Am.* **66**(3), 207–211 (1976).
 27. M. Clerc, "The swarm and the queen: towards a deterministic and adaptive particle swarm optimization," in *Evolutionary Computation, 1999. CEC 99. Proceedings of the 1999 Congress* (IEEE, 1999).
 28. L. Meynadier, V. Michau, M.-T. Velluet, J.-M. Conan, L. M. Mugnier, and G. Rousset, "Noise propagation in wave-front sensing with phase diversity," *Appl. Opt.* **38**(23), 4967–4979 (1999).
 29. N. Baba and K. Mutoh, "Measurement of telescope aberrations through atmospheric turbulence by use of phase diversity," *Appl. Opt.* **40**(4), 544–552 (2001).
 30. L. M. Mugnier, A. Blanc, and J. Idier, "Phase diversity: a technique for wave-front sensing and for diffraction-limited imaging," in *Advances in Imaging and Electron Physics* (Elsevier, 2006)
 31. N. A. Roddier, "Atmospheric wavefront simulation using Zernike polynomials," *Opt. Eng.* **29**(10), 1174–1180 (1990).
 32. D. L. Fried, "Statistics of a geometric representation of wavefront distortion," *J. Opt. Soc. Am.* **55**(11), 1427–1435 (1965).

1. Introduction

The phase diversity (PD) algorithm is a well-known algorithm to improve image quality, which has many applications in high resolution imaging and adaptive optics imaging [1–4]. To achieve near-diffraction-limited imaging, PD algorithm requires the collection of a simultaneous set of two (or more) focused images and defocused images. The focused images are the target image degraded by unknown wave-front aberrations, while the defocused images are the same blurred images, but with an additional known defocus wave-front. The reconstruction of unknown wave-front aberrations requires numerical processing to solve an optimization problem. The error metric, set as the optimization object, is built by the error intensity distribution between actually obtained image intensity and theoretical image intensity. The reconstruction of the parameterized wave-front aberrations can be obtained by minimizing the optimization objective function.

PD algorithm was first introduced by Gonsalves and Chidlaw [5]. This algorithm is suitable for point target and extended target at the same time. Since the work of Gonsalves and Chidlaw, scholars have used PD technique to estimate the wave-front aberrations induced by atmospheric blur or imperfections of the optical system and improve the quality of detected images [1, 2, 6, 7]. In recent years, PD algorithm has been successfully used in adaptive optics (AO) system [3, 4, 8–10]. Other applications of PD algorithm also include measurement of a laser beam [11, 12] and biological microscopy imaging [13].

However, it is not easy to apply PD algorithm to wave-front estimation due to the compli-

cated optimization processing, especially for large-scale wave-front sensing. The error metric is a multiple extreme values function on a multidimensional parameter space. When dealing with large-scale wave-front sensing, the global minimum search of error metric becomes extremely difficult. Gradient-based optimization algorithms, such as conjugate-gradient algorithm(CG) [14, 15] and quasi-Newton algorithm(BFGS) [16–19], are easily trapped in local minimums near the initial positions. Available global optimization algorithms used in PD, such as the genetic algorithm [20], have not focused on large-scale wave-front sensing. Moreover, general global optimization algorithms possess low convergence efficiency when dealing with large-scale wavefront sensing.

In this paper, we construct a two-step optimization algorithm(EPSo-BFGS) based on the combination of particle swarm optimization (PSO) [21–23] and Broyden-Fletcher-Goldfarb-Shanno (BFGS) algorithm. The kind of PSO used here(named EPSo) is a modified form of traditional PSO introduced a evolutionary mechanism, which is helpful to improve convergence efficiency. For the first step, EPSo provides global search and obtains a rough global minimum position in limited search steps. And for the second step, BFGS initialized by the rough global minimum position approaches the global minimum with high accuracy and fast convergence speed. EPSo-BFGS gives a guarantee of believable convergence efficiency and acceptable convergence speed.

The rest of this paper is organized as follows: In Section 2 we review the theory of PDPR. Section 3 describes the hybrid global optimization algorithm EPSo-BFGS. In Section 4 we discuss numerical simulations and a verification experiment. Finally, our conclusion and future work are given in Section 5.

2. Phase diversity phase retrieval

In this section, we briefly review the phase diversity technique. We will only consider two images separated by a certain defocus distance. Let us suppose that the object is illuminated with non-coherent quasi-monochromatic light, and the imaging system is a linear shift-invariant system [24]. The intensity distribution of the image plane with Gaussian noise can be modeled by the following equation:

$$i(\mathbf{r}) = o(\mathbf{r}) \otimes h(\mathbf{r}) + n(\mathbf{r}), \quad (1)$$

where \otimes stands for the convolution operation, \mathbf{r} is a two-dimensional position vector in the image plane, $o(\mathbf{r})$ is the object to be found, $h(\mathbf{r})$ is the point-spread function (PSF) of the optical system, and $n(\mathbf{r})$ is Gaussian noise. With the condition of near-field [25], the point-spread function associated with the focused image is given by

$$h(\mathbf{r}) = |FT^{-1}\{P(\mathbf{v}) \exp[j\phi(\mathbf{v})]\}|^2, \quad (2)$$

where FT^{-1} denotes the inverse Fourier transform, \mathbf{v} is a two-dimensional position vector in the pupil plane, $P(\mathbf{v})$ is the binary aperture function with values of 1 inside the pupil and 0 outside, and $\phi(\mathbf{v})$ is the unknown wave-front aberration. Similarly, the defocused image is given by

$$i_d(\mathbf{r}) = o(\mathbf{r}) \otimes h_d(\mathbf{r}) + n_d(\mathbf{r}), \quad (3)$$

and

$$h_d(\mathbf{r}) = |FT^{-1}\{P(\mathbf{v}) \exp[j(\phi(\mathbf{v}) + \phi_d(\mathbf{v}))]\}|^2, \quad (4)$$

where the subscript d indicates that a known phase diversity $\phi_d(\mathbf{v})$ has been added to the optical system. The common used $\phi_d(\mathbf{v})$ is defocus aberration. $\phi_d(\mathbf{v})$ can be exactly determined by the location of the defocused image plane relative to the focused plane.

The following error metric

$$\begin{aligned} E &= \sum_{\mathbf{u}} \tilde{E}(\mathbf{u}) \\ &= \sum_{\mathbf{u}} \{[I(\mathbf{u}) - O(\mathbf{u})H(\mathbf{u})]^2 + [I_d(\mathbf{u}) - O(\mathbf{u})H_d(\mathbf{u})]^2\} \end{aligned} \quad (5)$$

can evaluate the mean-squared image intensity difference between the data predicted by optical system and the data actually collected, where

$$\begin{aligned} O(\mathbf{u}) &= FT\{o(\mathbf{r})\}, \\ I(\mathbf{u}) &= FT\{i(\mathbf{r})\}, \quad I_d(\mathbf{u}) = FT\{i_d(\mathbf{r})\}, \\ H(\mathbf{u}) &= FT\{h(\mathbf{r})\}, \quad H_d(\mathbf{u}) = FT\{h_d(\mathbf{r})\}, \end{aligned} \quad (6)$$

\mathbf{u} is a two-dimensional spatial frequency coordinate, FT denotes the Fourier transform, $H(\mathbf{u})$ is the optical transfer function (OTF) of the focused system, and $H_d(\mathbf{u})$ is the OTF of the defocused system.

E is minimized by choice of $O(\mathbf{u})$ when

$$\frac{\partial \tilde{E}(\mathbf{u})}{\partial O} = 0, \quad (7)$$

namely,

$$O(\mathbf{u}) = \frac{H(\mathbf{u})I(\mathbf{u}) + H_d(\mathbf{u})I_d(\mathbf{u})}{|H(\mathbf{u})|^2 + |H_d(\mathbf{u})|^2}. \quad (8)$$

Substitution of $O(\mathbf{u})$ into E yields

$$E = \sum_{\mathbf{u}} \frac{|I(\mathbf{u})H_d(\mathbf{u}) - I_d(\mathbf{u})H(\mathbf{u})|^2}{|H(\mathbf{u})|^2 + |H_d(\mathbf{u})|^2}. \quad (9)$$

It is notable that Eq.(9) is independence of any object estimate.

In this paper, the unknown wave-front aberration is expanded on a finite set of Zernike polynomials [26]:

$$\phi(\mathbf{v}) = \sum_{j=4}^K a_j Z_j(\mathbf{v}). \quad (10)$$

The coefficients $a_1 - a_3$ stand for piston and tilt of the wave-front aberration, which have no effect on the resolution of image. The error metric E is therefore defined on a multidimensional parameter space:

$$\mathbf{a} = [a_4, a_5, \dots, a_K]. \quad (11)$$

For a given parameters \mathbf{a} , the error metric $E(\mathbf{a})$ can be calculated.

The goal is to find the optimal parameter set \mathbf{a} for which the error metric is globally minimum. Many standard gradient-based nonlinear optimization algorithms have been used by scholars, such as steepest decent algorithm(SD), conjugate-gradient algorithm(CG) and quasi-Newton algorithm(BFGS), etc. All gradient-based nonlinear optimization algorithms need an initial estimate for \mathbf{a} . Then the error metric and its gradient can be obtained at the initial estimate \mathbf{a} . The gradient of error metric can be calculated by finite difference method or by analytic expression [14]. The gradient provides a search direction, and a new estimate for \mathbf{a} is made along the search direction to find a smaller error metric. The entire procedure is repeated iteratively until a local minimum is found. In other words, the search of the optimal parameter set \mathbf{a} with gradient-based optimization algorithms is easily trapped in a local minimum that is not the true solution.

3. EPSO-BFGS optimization algorithm

To cope with the disadvantage that the existing gradient-based optimization algorithms used in PDPR are easily trapped in local minimums, we construct a hybrid EPSO-BFGS global optimization algorithm. This algorithm is based on the combination of Particle Swarm Optimization (PSO) and Broyden-Fletcher-Goldfarb-Shanno (BFGS) algorithm. EPSO is an improved form of traditional PSO, which a evolutionary mechanism has been introduced to improve convergence efficiency. Firstly, EPSO provides global search and obtains a rough global minimum position in finite search steps. Then, BFGS initialised by the rough minimum position approaches the global minimum with high accuracy and fast convergence speed.

Particle Swarm Optimization (PSO), belonging to the Evolutionary Algorithm family, is a population-based optimisation algorithm introduced by Kennedy and Eberhart [21]. Since PSO requires no gradient features, it is relatively flexible to be applied to PDPR. PSO employs a number of particles and each particle stands for a potential solution of the whole optimization problem. The initial position and velocity of each particle are randomly generated:

$$x^{(0)} = x^{(0)}(i, j) \quad (12)$$

$$v^{(0)} = v^{(0)}(i, j) \quad i = 1, \dots, N \quad j = 4, \dots, K \quad (13)$$

where N is the number of particles and K is the maximum number of design variables.

There are many kinds of modified PSO algorithms and we select the model of Clerc [27], which a constriction factor φ is introduced to improve convergence efficiency. The position and velocity of each particle are updated by the following equations:

$$v_{i,j}^{(n+1)} = \varphi \{v_{i,j}^{(n)} + c_1 r_1 [p_{i,l}^{(n)} - x_{i,j}^{(n)}] + c_2 r_2 [p_{i,g}^{(n)} - x_{i,j}^{(n)}]\}, \quad (14)$$

$$x_{i,j}^{(n+1)} = x_{i,j}^{(n)} + v_{i,j}^{(n+1)} \quad i = 1, \dots, N, \quad j = 4, \dots, K, \quad (15)$$

where

$$\varphi = \frac{2}{|2 - C - \sqrt{C^2 - 4C}|}, \quad C = c_1 + c_2, \quad C > 4. \quad (16)$$

In this work, we set $c_1 = c_2 = 2.05$. r_1 and r_2 are uniformly distributed random numbers between 0 and 1; $p_{i,l}$ is the best local position of particle i itself; $p_{i,g}$ is the best global position of particle i itself; $p_{i,l}$ and $p_{i,g}$ share information among all particles. $p_{i,l}$ and $p_{i,g}$ are updated as follows:

$$p_{i,l}^{(n+1)} = \begin{cases} p_{i,l}^{(n)}, & E(x_{i,j}^{(n+1)}) \geq E(p_{i,l}^{(n)}), \\ x_{i,j}^{(n+1)}, & E(x_{i,j}^{(n+1)}) < E(p_{i,l}^{(n)}). \end{cases} \quad (17)$$

$$p_{i,g}^{(n+1)} = p_{*,l}^{(n+1)}, \quad p_{*,l}^{(n+1)} \in \{p_{i,g}^{(n)}, p_{i,l}^{(n+1)}\}, \\ E(p_{*,l}^{(n+1)}) = \min\{E(p_{i,g}^{(n)}), E(p_{i,l}^{(n+1)})\}. \quad (18)$$

$$p_{i,g}^{(n+1)} = p_{*,l}^{(n+1)}, \\ p_{*,l}^{(n+1)} \in \{p_{i,g}^{(n)}, p_{i,l}^{(n+1)}\}, \\ E(p_{*,l}^{(n+1)}) = \min\{E(p_{i,g}^{(n)}), E(p_{i,l}^{(n+1)})\}. \quad (19)$$

We introduce a evolutionary mechanism to the PSO used here, namely, EPSO. Ascending sort of all error metrics reveals the performance of each particle. After the end of each search step, indexes of all particles are updated according to ascending sort. All particles are divided

into two parts: the front part and the rear part. The front part is possessed of more possibility than the rear part for the global minimum search of error metric E . The positions and velocities of the rear part are reset as the front part:

$$\begin{aligned} x_{i+N/2,j}^{(n+1)} &= x_{i,j}^{(n+1)}, \\ v_{i+N/2,j}^{(n+1)} &= v_{i,j}^{(n+1)} \quad i = 1, \dots, N/2, \quad j = 4, \dots, K. \end{aligned} \quad (20)$$

The mechanism can enhance the survival of advantageous particles and improve convergence efficiency.

A rough global minimum position $p_{i,g}^{(M)}$ can be obtained in limited search steps M by EPSO. The rough global minimum position provides a proper initial position for gradient-based optimization algorithms. We select a widely used quasi-Newton algorithm(BFGS) as the second step to approach the global minimum with high accuracy. BFGS algorithm is also suitable for multi-variable optimization problems.

In fact, for gradient-based optimization algorithms used in PDPR, a proper initial position is unknown and a zero position $\mathbf{a} = 0$ is usually initialized. Improper initial position is the very reason that gradient-based optimization algorithms are easily trapped in local minimums. EPSO-BFGS can avoid being trapped in a local minimum. The flow chart and sketch map for EPSO-BFGS are shown in Fig. 1 and Fig. 2.

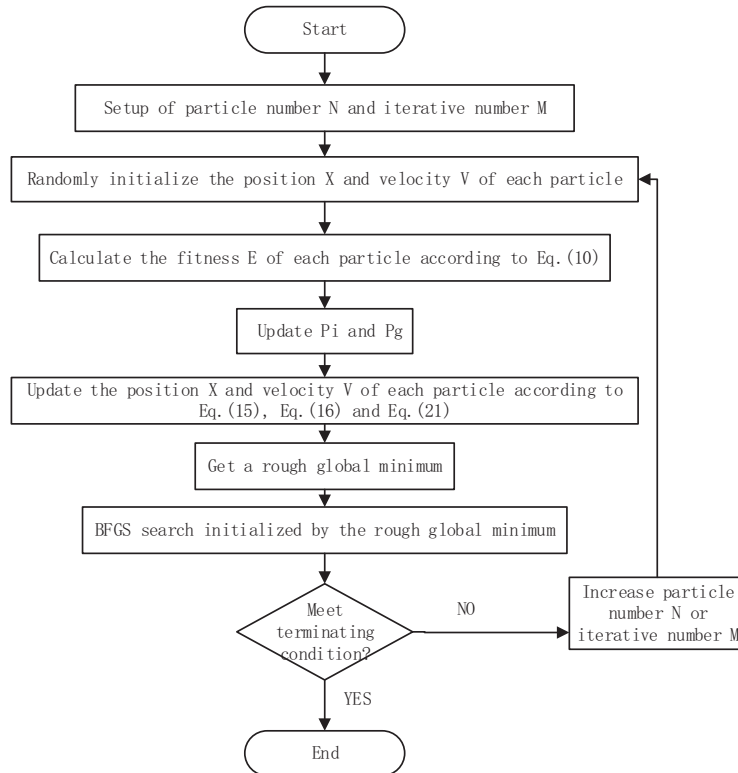


Fig. 1. Flow chart of EPSO-BFGS algorithm.

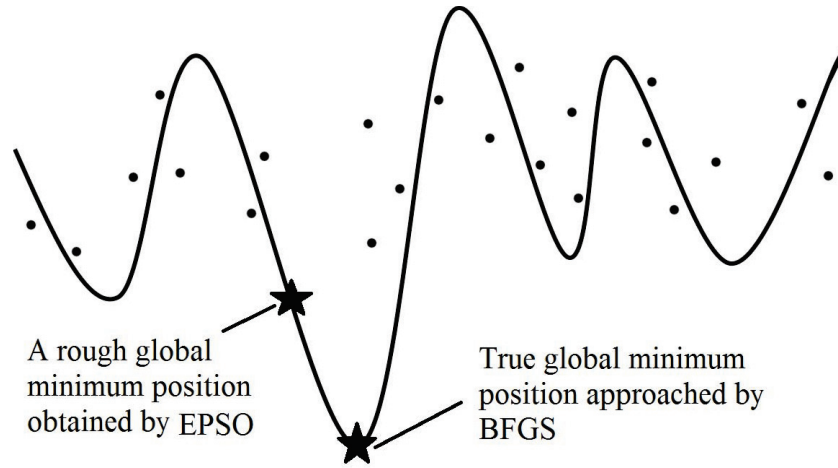


Fig. 2. Sketch map of EPSO-BFGS algorithm.

4. Numerical simulations and experimental results

4.1. Numerical simulations

In this section we describe and discuss the simulation results. We assume all images are Nyquist sampled. The size of each data frame is 200×200 pixels and the intensity levels are quantized to 16 bits. The diameter of the pupil is set to 100 pixels. The amount of defocus used for the phase diversity is set to be 1.0λ peak to valley (PV), which is commonly used [28–30]. Zernike polynomials are used here up to the fifteenth term, so the computed parameter space is

$$\mathbf{a} = [a_4, a_5, \dots, a_{15}]. \quad (21)$$

The simulated wave-front aberration ϕ_{true} is Kolmogorov aberrated and generated in the pupil plane by the work of Noll and Roddier [26, 31], which lets us easily adjust the turbulence strength D/r_0 , where D is a simulated telescope diameter and r_0 is Fried's parameter [32]. The rms value of simulated wavefront is defined as follows:

$$RMS\{\phi_{true}\}(\lambda) = \frac{1}{2\pi} \left[\sum_{\mathbf{v}} (\phi_{true}(\mathbf{v}) - \phi_{aver}(\mathbf{v}))^2 / N_T \right]^{\frac{1}{2}}, \quad (22)$$

where ϕ_{aver} is the average wave-front of ϕ_{true} , N_T is the total number of pixels within the pupil aperture. The accuracy of the reconstructed wavefront ϕ is quantified with the rms phase error between the true wave-front aberration and the reconstructed wave-front aberration. The definition of rms phase error is

$$RMS \text{ error}(\lambda) = \frac{1}{2\pi} \left[\sum_{\mathbf{v}} (\phi(\mathbf{v}) - \phi_{true}(\mathbf{v}))^2 / N_T \right]^{\frac{1}{2}}. \quad (23)$$

We will firstly show the different performances between three widely used gradient-based optimization algorithms (SD, CG and BFGS) and our hybrid algorithm EPSO-BFGS. In the case of different turbulence strength D/r_0 , Table 1 lists the RMS errors achieved by SD, CG, BFGS and EPSO-BFGS algorithms. Each RMS error is the average value of three same calculation cases. As indicated before, the initial condition of SD, CG and BFGS algorithms is $\mathbf{a} = 0$. When the turbulence strength $D/r_0 = 1$, the three gradient-based optimization algorithms work equally

well as EPSO-BFGS algorithm. However, when dealing with large turbulence strength, the three gradient-based optimization algorithms obviously lost much accuracy of calculation. Comparatively, EPSO-BFGS algorithm can accurately recover the simulated wave-front aberrations of several large turbulence strength D/r_0 .

Table 1. RMS errors(λ) achieved by SD, CG, BFGS and EPSO-BFGS algorithms for wave-front aberrations of different D/r_0 .

	Algorithms			
	SD	CG	BFGS	EPSO-BFGS
$D/r_0 = 1$	0.0129	0.0127	0.0193	0.0132
$D/r_0 = 5$	0.0348	0.0838	0.0385	0.0012
$D/r_0 = 10$	0.0429	0.1529	0.2989	0.0048
$D/r_0 = 15$	0.1549	0.3340	0.2974	0.0017
$D/r_0 = 20$	0.3012	0.3199	0.3454	0.0093

Similarly, in Table 2 and Fig. 3, we show the performances of SD, CG, BFGS and EPSO-BFGS algorithms dealing with wave-front sensing of different RMS. Each RMS error is the average value of three same calculation cases. From the initial position $\mathbf{a} = 0$, SD, CG and BFGS algorithms carry on the search for the global minimum position. When the RMS value of unknown wave-front is 0.1λ , SD, CG and BFGS algorithms are able to obtain satisfactory RMS errors. That means the PDPR optimization problem is probable convex optimization for small-scale wave-front sensing and SD, CG and BFGS algorithms are competent.

Table 2. RMS errors(λ) achieved by SD, CG, BFGS and EPSO-BFGS algorithms for wave-front aberrations of different RMS.

	Algorithms			
	SD	CG	BFGS	EPSO-BFGS
RMS= 0.1λ	0.0247	0.0379	0.0239	0.0015
RMS= 0.2λ	0.0512	0.1161	0.1139	0.0005
RMS= 0.3λ	0.1231	0.0935	0.2384	0.0004
RMS= 0.4λ	0.2087	0.2919	0.3171	0.0359
RMS= 0.5λ	0.4485	0.3993	0.4474	0.0181
RMS= 0.6λ	0.5554	0.4848	0.5393	0.0474
RMS= 0.7λ	0.5802	0.6219	0.6934	0.0344
RMS= 0.8λ	0.6924	0.6993	0.7497	0.0129

However, when dealing with large-scale wave-front aberrations, Table 2 and Fig. 3 reveal the fact that the search of SD, CG and BFGS algorithms only go ahead a short distance. PDPR optimization problem is non-convex and complicated for large-scale wave-front sensing and SD, CG and BFGS algorithms are easily trapped in a local minimum. The initial position and velocity of EPSO-BFGS algorithm are randomly initialized. And the global search mechanism of EPSO-BFGS algorithm ensures a more optimal position approach than all local minimum positions, that is, a rough global minimum position. The rough global minimum position provides a proper initializing position for BFGS algorithm. RMS errors obtained by EPSO-BFGS algorithm are remarkably smaller than other algorithms. The excellent performance of EPSO-BFGS algorithm confirms the validity and robustness of our mechanism of EPSO-BFGS algorithm.

It is notable that BFGS algorithm, as the second step of EPSO-BFGS algorithm, plays an important role for the second approach after initialized by the rough global minimum position obtained by EPSO. Table 3 is a list of RMS errors achieved by EPSO and EPSO-BFGS

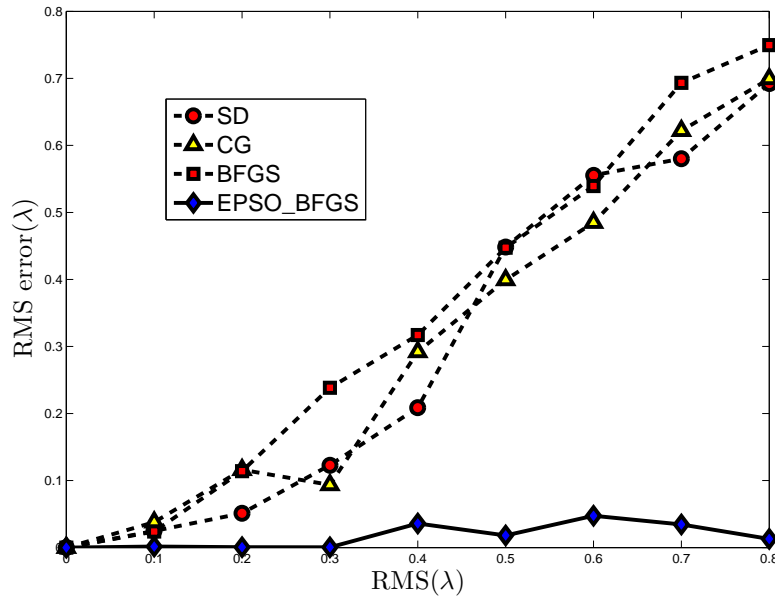


Fig. 3. RMS errors chart with SD, CG, BFGS and EPSO-BFGS algorithms for wave-front aberrations of different RMS.

algorithms for different particle number N and iteration number M . The coefficients \mathbf{a} used here ($\text{RMS}=0.1619\lambda$, $\text{PV}=1.0310\lambda$) is case1 listed in Table 4. We can see that BFGS algorithm can obviously improve the performance of EPSO when particle number N and iteration number M are small. A proper initial position can be obtained by EPSO algorithm when particle number N and iteration number M are big enough, which ensures that BFGS algorithm searches the global minimum position towards the unknown wave-front (RMS errors fluctuate near 0.017λ). For the cases that RMS errors obtained by EPSO-BFGS fluctuate near 0.017λ confirm the validity of EPSO-BFGS. We would like to point out that the complementary role of BFGS is weak when particle number N and iteration number M are big enough. Even so, we think that BFGS algorithm is indispensable because better performance is always desired.

Table 3. RMS errors(λ) achieved by EPSO and EPSO-BFGS algorithms for different particle number N and iteration number M .

	M=5		M=20		M=50		M=100	
	EPSO	EPSO-BFGS	EPSO	EPSO-BFGS	EPSO	EPSO-BFGS	EPSO	EPSO-BFGS
N=5	0.18466	0.12780	0.13181	0.03237	0.15558	0.02036	0.08712	0.01680
N=20	0.09797	0.01716	0.04689	0.01711	0.02198	0.01732	0.02835	0.01738
N=50	0.09206	0.01917	0.04455	0.01756	0.02035	0.01738	0.01857	0.01732
N=100	0.08397	0.02045	0.03251	0.01747	0.01752	0.01737	0.01744	0.01737

Finally, we will show the ability of EPSO-BFGS algorithm for large-scale wave-front sensing. The coefficients \mathbf{a} used here for simulations are listed in Table 4, of which case2 ($\text{RMS}=1.0\lambda$, $\text{PV}=5.8325\lambda$) and case3 ($\text{RMS}=1.2\lambda$, $\text{PV}=8.6304\lambda$) are large-scale wave-front aberrations. Reconstructed coefficients \mathbf{a} for case2 and case3 are also listed in Table 4. And in Fig. 4 and Fig.

5, phase retrieval and reconstructed object are given. It can be seen that high accuracy can be achieved by EPSO-BFGS algorithm for the two large-scale wave-front aberrations, where the RMS phase errors are 0.01092λ and 0.00096λ , respectively. The simulation results confirm the capability of our EPSO-BFGS algorithm for large-scale wave-front sensing.

Table 4. Coefficients of three cases used for simulations. Case1 is used for the simulations in Tab.3. Case2 and case3 are large-scale phases for the simulations of Fig. 4 and Fig. 5.

Coefficient	Case1	Case2	Case3		
	Set	Set	Reconstructed	Set	Reconstructed
a_4	0.9361	-4.2028	-4.1423	-3.9998	-3.9961
a_5	0.3538	1.5276	1.5149	-0.9988	-0.9987
a_6	0.1681	-4.2380	-4.2213	4.1653	4.1604
a_7	0.3767	-1.3286	-1.3350	4.8879	4.8899
a_8	0.2782	0.0151	0.0343	0.9817	0.9822
a_9	0.2210	-2.3758	-2.3585	-3.3273	-3.3289
a_{10}	-0.0919	1.8187	1.8219	1.5528	1.5512
a_{11}	-0.0653	-0.0623	-0.0472	0.5909	0.5912
a_{12}	0.0093	-0.8079	-0.7997	0.3772	0.3766
a_{13}	0.0375	-1.6907	-1.6975	1.1993	1.1994
a_{14}	0.1464	0.0124	-0.0159	0.4065	0.4068
a_{15}	0.1284	0.1198	0.1367	-0.6608	-0.6612

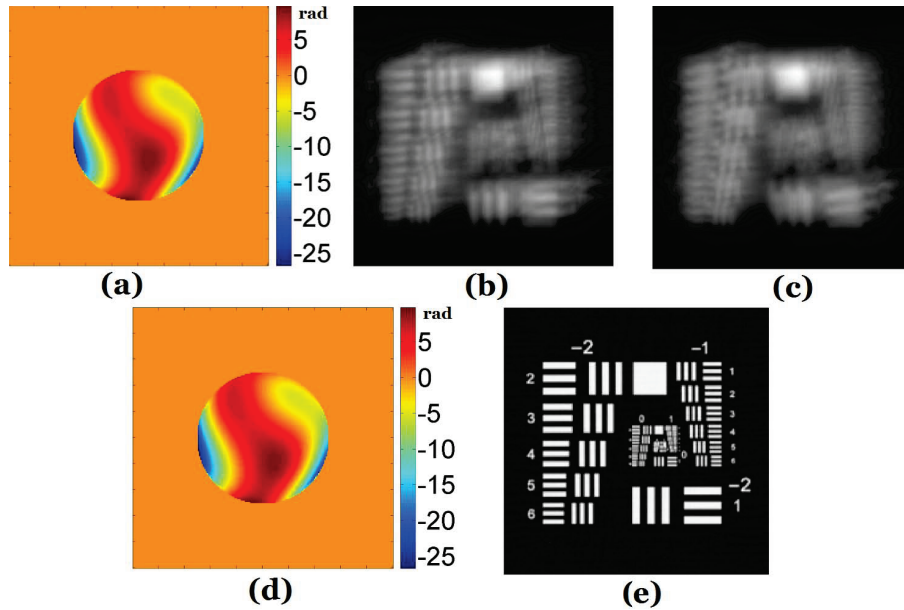


Fig. 4. Simulation results of phase retrieval and reconstructed for the phase aberration of $\text{RMS}=1.0\lambda$, $\text{PV}=5.8325\lambda$. (a) and (d) are the simulated and reconstructed phases respectively, where the RMS phase error is 0.01092λ . (b) and (c) are the simulated focused and defocused images, respectively. (e) is the reconstructed object.

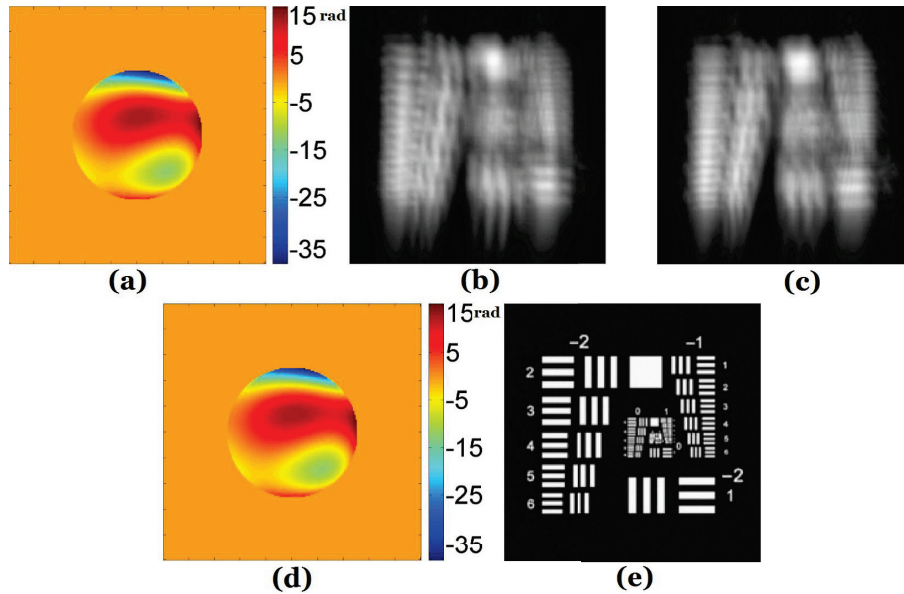


Fig. 5. Simulation results of phase retrieval and reconstructed for the phase aberration of $\text{RMS}=1.2\lambda$, $\text{PV}=8.6304\lambda$. (a) and (d) are the simulated and reconstructed phases respectively, where the RMS phase error is 0.00096λ . (b) and (c) are the simulated focused and defocused images, respectively. (e) is the reconstructed object.

4.2. Experimental results

A preliminary experiment has been made to test the practical performance of EPSO-BFGS for PDPR. The simplified block diagram of the optical system used here is shown in Fig. 6. The equivalent focal length F is 300mm , the pupil diameter D is 10mm , and the CCD(Andor zyla 4.2) pixel size is $6.5\mu\text{m}$. A common halogen lamp is selected as the light source. A fiber bundle is used as the extended object to be measured. To obtain quasi-monochromatic image, a filter(633nm) is located at the collimated beam. Lens L1 is used to collimate the light from the fiber. The collimated beam proceeds through the fiber, a beam splitter, a artificial deformed mirror and reflected by the beam splitter. Some unknown aberrations are introduced to the optical system by adjusting the deformation of the mirror. After passing through the lens L2, the focal images with aberrations can be obtained by the CCD located at the focal plane. Then, we move the CCD by the distance d to get the the defocused images. The corresponding peak-to-valley optical path difference Δ [30] is equal to

$$\Delta = \frac{d}{8(F/D)^2}. \quad (24)$$

As we have mentioned in our numerical simulations that choosing d such that $\Delta = \lambda$ is a relatively better choice to obtain accurate results. So the distance d here is 4.5576mm . The measured object takes the area of 300×300 pixels and the exposure time is 20ms .

The computed parameter space is $\mathbf{a} = [a_4, a_5, \dots, a_{15}]$, the same as our numerical simulations above. The size of measured object is larger than our numerical simulations, which means more computational cost. To get believable results, we set particle number $N = 500$ and iteration number $M = 500$. After the parameter estimates of the unknown phase aberrations, we still

need to employ a Wiener-Helstrom noise filter [14] to perform the object restoration:

$$O(\mathbf{u}) = \frac{H(\mathbf{u})I(\mathbf{u}) + H_d(\mathbf{u})I_d(\mathbf{u})}{|H(\mathbf{u})|^2 + |H_d(\mathbf{u})|^2 + P_n(\mathbf{u})/P_f(\mathbf{u})}. \quad (25)$$

where the third term in the denominator is the ratio of the power spectral density of the noise to that of the object. The reconstructed image is then obtained by the inverse Fourier transform of $O(\mathbf{u})$. In fact, It is difficult to get the power spectral density of the noise and that of the object. Usually, a common approach is to assume the ratio to be a small constant.

We will firstly compare the performances of different optimization algorithms used in PDPR for a simple large-scale wave-front sensing, that is, a 2λ (PV) defocus aberration. We make the deformation of the mirror zero, and the "focal" image is obtained by moving the CCD by the distance $2d$, which means a 2λ (PV) defocus aberration is added to the optical system. Then, the defocused image is obtained by moving the CCD by the distance d again. As shown in Fig. 7, we can see from the reconstructed image that the performances of SD, CG and BFGS algorithms are poor. The three gradient-based optimization algorithms provide similar wrong phase sensing. As we have pointed out in our numerical simulations, SD, CG and BFGS algorithms are easily trapped in a local minimum for PDPR. In comparison, EPSO-BFGS algorithm provides a satisfactory performance. Although there are still some small errors, the reconstructed phase by EPSO-BFGS is quite similar with a defocus aberration. We have found the computed parameter a_4 (stands for defocus aberration) is 2.059λ (PV).

To testify the effectiveness of EPSO-BFGS algorithm, three different random wave-front aberrations are generated by the deformed mirror. Reconstructed wavefront aberrations and images are shown in Fig. 8. The three measured wavefront aberrations are (a)(RMS= 0.155λ , PV= 0.765λ), (b)(RMS= 0.261λ , PV= 1.389λ) and (c)(RMS= 0.416λ , PV= 2.136λ), respectively. Experimental results are satisfying and practically prove the feasibility of the proposed EPSO-BFGS algorithm for PDPR.

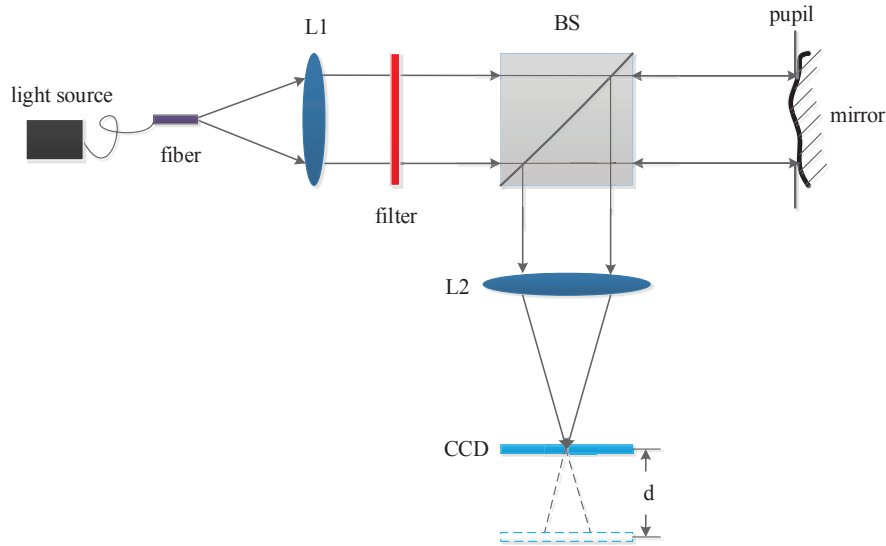


Fig. 6. Simplified block diagram of the verification experiment system of PDPR.

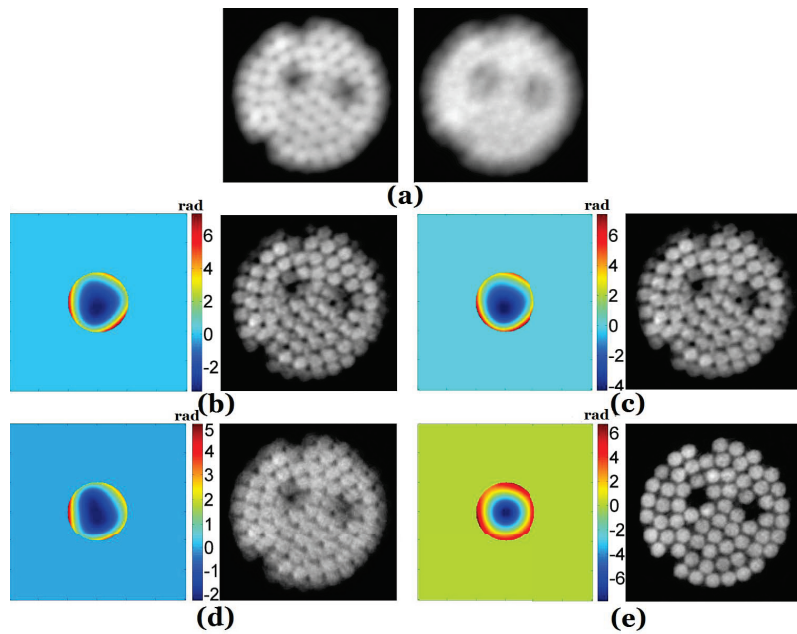


Fig. 7. Experimental results of PDPR for a 2λ (PV) defocus wave-front aberration. (a) contains the focal image(left) and the defocused image(right) collected by the CCD. (b),(c),(d) and (e) show the phases and images reconstructed by SD, CG, BFGS and EPSO-BFGS, respectively.

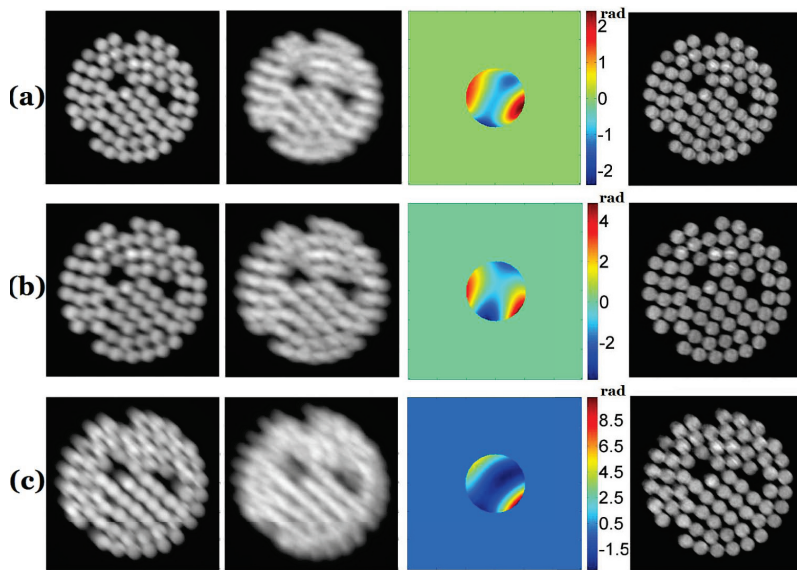


Fig. 8. Experimental results of PDPR for three different wave-front aberrations by EPSO-BFGS. (a),(b) and (c) contain the the focal image, the defocused image, reconstructed phase and images, respectively.

5. Conclusion

In this paper, we construct a hybrid EPSO-BFGS global optimization algorithm for PDPR. The two-step mechanism of EPSO-BFGS algorithm overcomes the shortcomings that traditional gradient-based optimization algorithms are easily trapped in local minimums. At the same time, EPSO-BFGS algorithm is stable and reliable. Also, the formulas of EPSO-BFGS algorithm is simple and easy to implement. Computer simulations illustrate that this algorithm can cope with various scales of wave-front sensing. And for large-scale wave-front sensing, EPSO-BFGS can also obtain satisfactory performance. The performed experiment confirms the effectiveness of EPSO-BFGS. Our work provide a practicable algorithm for the complicated nonlinear optimization processing of PDPR, which could enhance the ability of PDPR technique used in several fields such as high resolution imaging and adaptive optics imaging. As part of our future work, we are interested in the physical mode of PDPR. It is desired to find an modified form of the error metric to improve the convergence of PDPR.

Funding

National Science Foundation of China (NSFC) (6147515) and 61405194); Science Foundation of State Key Laboratory of Applied Optics.